

Could high-speed civil transport aircraft impact stratospheric and tropospheric temperatures measured by microwave sounding unit?

Kathryn Pierce Shah and David Rind¹

Center for Climate Systems Research, Columbia University, NASA Goddard Institute for Space Studies, New York

Patrick Lonergan

Science Systems and Applications, Inc., New York

Abstract. A radiative transfer postprocessor calculates microwave brightness temperatures T_b from climate experiments investigating supersonic aircraft exhaust impacts with the Global Climate/Middle Atmosphere Model (GCMAM) at the NASA Goddard Institute for Space Studies. Microwave signals from the exhaust-perturbed GCMAM atmospheres are contrasted with observed interannual variability (natural “noise”) for 1982–1991 as measured by microwave sounding unit (MSU) channels across the lower troposphere, midtroposphere, and lower stratosphere. Exaggerated ozone and water vapor perturbations at supersonic cruise altitudes produce microwave signals easily detected against natural noise. Removal of ozone greenhouse action between 200 and 50 hPa cools all MSU channels with greatest ΔT_b of -8.3 K and signal-to-observed-noise (S/N) ratios above 20 in the lower stratospheric channel. Doubling middle-atmospheric water vapor above 100 hPa cools lower stratospheric T_b values by 1.5 K while warming tropospheric channels, particularly the tropopause channel. Detectable S/N ratios of 2–4 occur over the tropics and subtropics in the lower-to-middle troposphere and lower stratosphere. Realistic ozone and water vapor perturbations are based on the High-Speed Research Program/Atmospheric Effects of Stratospheric Aircraft reports. These realistic stratospheric ozone and water vapor changes produce ΔT_b signals under 0.6 K and negligible S/N ratios. The slight climatic forcings are overwhelmed by natural feedbacks of high and low cloud formation, sea ice formation, and snow coverage. Thus the modeled realistic ozone and water vapor perturbations produce small and conflicting microwave signals, undetectable against natural variability and other sources of anthropogenic climatic forcing.

1. Introduction

Aircraft emissions can possibly change the regional and global climate through their greenhouse interaction with radiation and their photochemical interaction with ambient atmospheric species. Supersonic aircraft add water vapor, NO_x , CO_2 , sulfur, soot, and cloud condensation nuclei to high altitudes (18–21 km) in the stratosphere. The greenhouse influence of exhaust constituents such as water vapor is enhanced in the upper troposphere and lower stratosphere due to colder ambient temperatures. Nitrogen oxides from supersonic exhaust drive homogeneous catalysis of ozone, altering its vertical distribution.

The number of supersonic flights is expected to increase sharply with a proposed high-speed civil transport fleet (HSCT) [*High-Speed Research Program/Atmospheric Effects of Stratospheric Aircraft (HSRP/AESA)*, 1993]. In Boeing and McDonnell Douglas forecasts, projected passenger demands re-

quire a fleet of 500 Mach 2.4 HSCTs in 2015 [*HSRP/AESA*, 1993]. Supersonic air traffic will mostly be located in current high-concentration corridors, in the northern hemisphere between 40° and 50° N. NO_x emissions from the 2015 subsonic and HSCT fleets are estimated to double 1990 levels of NO_x emission in the lower stratosphere (10–13 km) and add new NO_x amounts to the stratosphere (19–21 km).

Consequently, a series of Goddard Institute for Space Studies (GISS) Global Climate/Middle Atmosphere Model (GCMAM) experiments have begun investigating the climatic impact of projected 2015 supersonic aircraft exhaust [Rind and Lonergan, 1995]. Rind and Lonergan [1995, 7381] concluded that the exhaust experiments “emphasize that stratospheric changes affect tropospheric dynamics in the model, that tropospheric changes can affect stratospheric dynamics, and that tropospheric feedback processes and natural variability are important when assessing the climatic response to aircraft emissions.” The next step is to follow the lead of these GCMAM forecasts and to assess the significance of forecast supersonic impacts against observed, natural atmospheric variability. New complementary tools, a microwave postprocessor to the GCMAM and microwave satellite observations, make such an assessment possible.

Microwave sounding units (MSUs) aboard NOAA polar or-

¹Also at NASA Goddard Institute for Space Studies, Goddard Space Flight Center, New York.

Copyright 1996 by the American Geophysical Union.

Paper number 96JD02721.
0148-0227/96/96JD-02721\$09.00

Table 1. GCMAM Supersonic Aircraft Experiments

GCM Run	Length	Description
Control run	50-year run	Ozone of Figure 1 (left) [Rind <i>et al.</i> , 1988a, b]
Exaggerated exhaust		
Ozone	30-year run	Remove ozone between 200 and 50 hPa
Water vapor	30-year run	Double water vapor to 6.0 ppmv above 100 hPa
Realistic exhaust		
Ozone	30-year run	Ozone changes of Figure 1 (right)
Water vapor	50-year run	Add 0.2 ppmv water vapor above 100 hPa

biters since 1978 have provided brightness temperature T_b climatologies. These microwave radiometers have two features that are attractive to climate research: global coverage and consistent instrumentation. The MSU channels sense separate altitude regions relevant to climate concerns: Channel 4 captures information on altitudes affected by stratospheric ozone change (~ 17 km), channel 3R captures information on near-tropopause convection heights (~ 11 km), and channels 2 and 2R capture information on tropospheric anthropogenic warming and El Niño-Southern Oscillation (ENSO) events (~ 5 and ~ 2 km, respectively). These climatologies will be extended with higher spatial and frequency resolution upon launch of the Advanced Microwave Sounding Units (AMSUs) series in the late 1990s [Goldberg and Fleming, 1995]. The AMSU will sample in twelve oxygen channels sounding altitudes from the surface into the lower thermosphere (~ 85 km) with 50-km, nadir footprints [Rosenkranz *et al.*, 1994; Saunders, 1993].

The microwave postprocessor to the GCMAM calculates global maps of microwave emission from a GCMAM's predicted climate [Shah and Rind, 1995]. It creates a path for direct comparison of a predicted model atmosphere to satellite microwave observations of the real atmosphere and its variability. The GCMAM experiments focused on two influential perturbations, the impact of water vapor and ozone differences from supersonic aircraft exhaust [Rind and Lonergan, 1995]. The resulting GCMAM microwave maps can comment on the aircraft exhaust's microwave signature relative to natural microwave variability, direct monitoring to sensitive locales and vertical regimes, and inform future instrument designs of necessary resolution and signal capabilities for monitoring of unwanted supersonic aircraft exhaust impacts.

2. GCMAM Supersonic Ozone and Water Vapor Experiments

The Global Climate/Middle Atmosphere Model investigated supersonic aircraft ozone and water vapor impacts through a series of equilibrium experiments [Rind and Lonergan, 1995]. First, exaggerated perturbations of stratospheric ozone and water vapor were tested to find the gross resulting patterns of dynamic and climatic responses of the atmosphere. Sea surface temperatures (SSTs) were held fixed and then were allowed to change in separate experiments. This singled out the direct, in situ radiative impact of altering stratospheric ozone or water vapor from the impacts of feedbacks and tropospheric responses. Second, realistic ozone and water vapor perturbations estimated for potential aircraft exhaust by the year 2015 [HSRP/AESA, 1993] were run to find a more realistic atmospheric response against the "backdrop" of natural variability in the GCMAM.

The Global Climate/Middle Atmosphere Model has 23 ver-

tical layers spread from the surface to a rigid top in the lower mesosphere at roughly 85 km or 1 μ b. It has horizontal resolution of 8° latitude by 10° longitude and all of the regular components of a climate model (i.e., calculation of cloud cover, snow cover, sea ice, surface albedo, etc.) [Rind *et al.*, 1988a, b]. The GCMAM can calculate sea surface temperatures in climate change experiments for an ocean with a maximum mixed layer of 65 m depth and specified ocean heat transports [Hansen *et al.*, 1984]. Stratospheric gravity wave drag arises through model parameterizations forced by topography, convection, and wind shear. This middle-atmosphere model has been used previously to investigate climate change experiments involving anthropogenic greenhouse gases and volcanic aerosols [Rind *et al.*, 1990, 1992].

Microwave emission's interannual variability in the GCMAM is less than that observed by MSU. This is sensible given the lack ENSO forcing via observed SSTs, reduced occurrence of lower stratospheric warming events, and omission of volcanic forcing in the GCMAM control run. Consequently, the tropospheric variability for channels 2 and 2R is at best half the observed value at equatorial latitudes and especially over the Pacific. In the lower stratosphere the climate model's variability is half the observed value over southern high latitudes and one third the observed value over northern high latitudes. However, the GCMAM's microwave interannual variability does increase with higher latitude, does increase over northern continents, and does heighten significantly at 60°S similar to MSU observations. The microwave signals determined for the supersonic exhausts in section 5 are consequently more significant relative to the GCMAM's interannual variability than the observed variability. Rind *et al.* [1988b] discusses the GCMAM variability performance in depth with regard to other observables.

The GCMAM's exaggerated perturbation experiments explored the dynamic and climatic manner of responses, while the realistic perturbations led to more subtle impacts. This paper examines the microwave emission from a subset of the GCMAM experiments as outlined in Table 1.

The influence of reduced ozone depends on its distribution over altitude and, to a lesser extent, on the latitude and season. Decreasing ozone in the troposphere and lower stratosphere decreases atmospheric greenhouse ability and cools the climate. Decreasing ozone in the middle and upper stratosphere, on the other hand, increases transmission of shortwave solar radiation to the ground and warms the climate [Lacis *et al.*, 1990]. Water vapor from supersonic exhaust is expected to cool temperatures at flight altitudes and potentially warm the surface climate as it is a major greenhouse gas. Supersonic water vapor can potentially produce significant effects, as water vapor impacts have been found to be greatest when perturbations occur near the tropopause [Rind and Lacis, 1993].

The exaggerated ozone experiment removed all ozone from

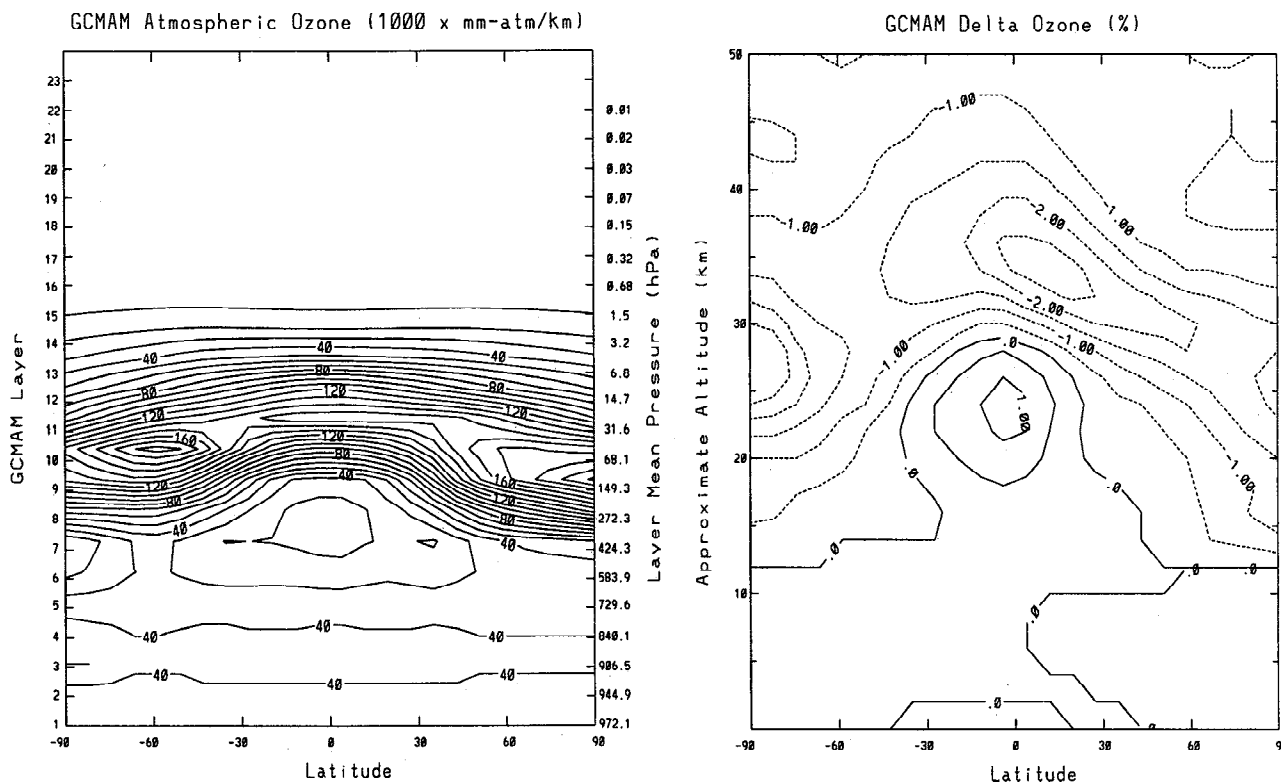


Figure 1. (left) Ambient ozone concentrations in the Global Climate/Middle Atmosphere Model (GCMAM) control run [McPeters, 1993] and (right) realistic ozone perturbations in the GCMAM experiments series on supersonic aircraft emission (Figure 8a corrected and Figure 8b from Rind and Lonergan [1995]).

the lower stratosphere between 200 and 50 hPa (or, equivalently, between 12 and 20 km). The exaggerated water vapor experiment doubled the middle atmosphere's water vapor from regular 3 to 6 parts per million by mass (ppmm) above 100 hPa (above 17 km).

Realistic ozone and water vapor perturbations were based on a 2015 scenario of 500 supersonic aircraft flying at Mach 2.4 with an NO_x emission index (EI) of 15 with modified subsonic aircraft schedules. This 2015 scenario is outlined in the High-Speed Research Program/Atmospheric Effects of Stratospheric Aircraft reports [HSRP/AESA, 1993].

Realistic ozone perturbations were globally input as slight tropospheric and lower stratospheric increases (with a maximum increase of 1% in the tropics about 22 km) and higher-altitude decreases (with a minimum at -2.5% in the tropics about 35 km) as shown in Figure 1. These ozone perturbations were based on results from the two-dimensional Goddard Space Flight Center (GSFC) photochemical model and generally agree with results from other photochemical models [HSRP/AESA, 1993; Rind and Lonergan, 1995].

Realistic water vapor perturbations were input as a global change to the GCMAM's middle-atmospheric water vapor of $+0.2$ ppmm above 100 hPa (an increase of 7% above 17 km). This perturbation is the globally averaged change of an 0.8 parts per million by volume (ppmv) increase in water vapor in flight corridors estimated from the supersonic fleet of 500, EI 15, Mach 2.4 aircraft. This perturbation does not include water vapor changes associated with subsonic aircraft and has large uncertainties from problematic stratosphere-troposphere transport.

With the microwave radiative transfer postprocessor, micro-

wave maps of the perturbed and the control GCMAM atmospheres are calculated. This analysis assesses supersonic aircrafts' microwave signals relative to current MSU data and can provide implications for future AMSU observations.

3. MSU Data on Annual Timescales

The current MSU channels 2 (53.74 GHz or 5.58 mm), 3 (54.96 GHz or 5.46 mm), and 4 (57.95 GHz or 5.18 mm) simultaneously measure atmospheric temperatures in the midtroposphere, the tropopause region, and the lower stratosphere, respectively. These channels have 200-MHz bandwidths on the low-frequency side of the 60-GHz molecular oxygen band. The MSU has collected brightness temperatures T_b continuously since 1978 in swaths having a nadir, 110-km-circular footprint and an elliptical, 210-km-wide footprint at the extreme viewing angle of 47.5° . These footprints accumulate to global coverage every several days given a particular satellite's precession rate. Resultant MSU climatologies of monthly mean T_b maps and complementary monthly anomaly T_b maps, created by Spencer and Christy [1992a, b], are gridded to 2.5° resolution. This MSU 2.5° horizontal resolution is finer than or comparable to most atmospheric climate models' horizontal resolutions.

Figure 2 shows the broad temperature weighting functions for MSU channels 2, 2R, 3R, and 4 centered around 800 hPa (2 km), 600 hPa (5 km), 270 hPa (11 km), and 80 hPa (17 km), respectively. Synthesized channels 2R and 3R measure narrower atmospheric regions with vertical positions dependent upon their source, a mix of viewing angles of an MSU channel or a mix of MSU channels. Channel 2R is a mixture of channel

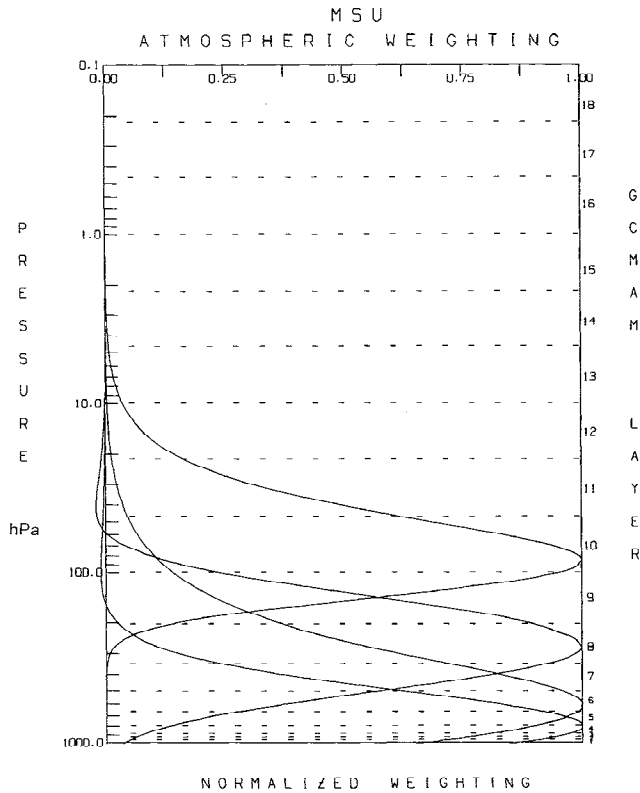


Figure 2. Normalized nadir temperature weighting functions for microwave sounding unit (MSU) channels 4, 3R, 2, and 2R from a U.S. Standard Atmosphere and a land emissivity of 1.0. The Goddard Institute for Space Studies (GISS) GCMAM's 23 vertical layers are indicated.

2 T_b at different view angles: 4 times the average of channel 2 T_b at 28.41° and 18.94° minus 3 times the average of T_b at 47.35° and 37.88° . Channel 3R is a combination of frequency

channels: 1.35 times a nadir channel 3 T_b minus 0.35 times a nadir channel 4 T_b . Channel 3R's climatology has just become publicly available and promises valuable contributions to climate research given its sensitivity to conditions about the tropopause. The MSU channels' broad vertical weightings are quite useful as they encompass several layers in the GISS GCMAM.

Figure 3 shows the global annual mean and interannual variability T_b maps from MSU. These MSU channel maps were generated from the valuable monthly mean and monthly anomaly MSU climatologies over the period of 1982–1991 produced by *Spencer and Christy* [1992a, b]. The microwave channels are nearly insensitive to the presence of clouds. Table 2 lists cloud influences on T_b for relevant MSU channels based on one-dimensional radiative transfer calculations (as discussed by *Shah and Rind* [1995]). Precipitation influences, which would cool T_b values by several degrees, were filtered from the original climatologies [*Spencer and Christy*, 1992a, b; *Christy and Drouhilet*, 1993].

Global annual-average maps of the four channels, 2R, 2, 3R, and 4, in Figure 3 illustrate the greater range in T_b for tropospheric channels nearer the ground versus the relatively muted range in T_b for the tropopause and lower stratospheric channels. Maps of mean channel 2 and 2R T_b show familiar temperature gradients with warmest T_b values about the equator and over low topography. MSU channel 4 maps, on the other hand, show lower stratospheric conditions with cool poles, colder equatorial latitudes, and wave energy present in its warm midlatitudes. MSU channel 3R maps are a mixture of tropospheric and stratospheric conditions, and its annual-average map presents a bland, warm tropics and subtropics with cooler poles.

The observed interannual variability T_b maps (Figure 3) reflect atmospheric conditions over the time period of 1982–1991. Future atmospheric variability is assumed to resemble these maps to first degree.

Each MSU channel typically experiences greatest variability

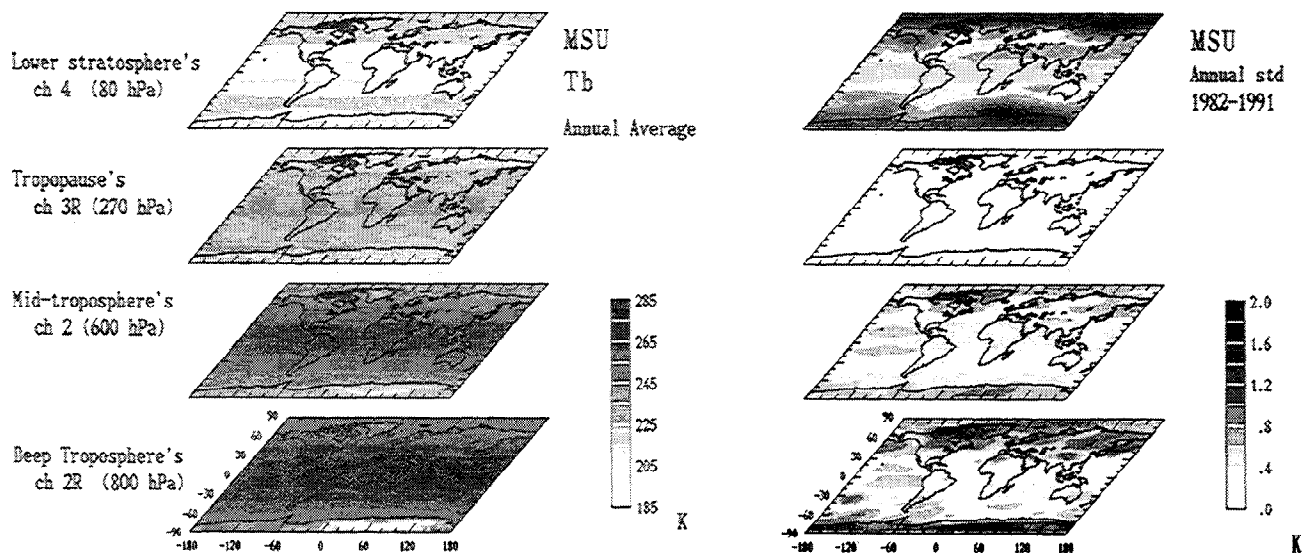


Figure 3. (left) Annual mean and (right) interannual variability T_b maps from MSU channels 2R, 2, 3R, and 4 with associated peak weighting pressures noted. Channel 3R's map is based on preliminary data generously provided by R. Spencer (private communication, 1994) for the 1982–1991 period. Channel 3R's global variability map is not yet available. The other channel maps are based on the monthly mean and anomaly MSU climatologies produced by *Spencer and Christy* [1992a, b] based on the 1982–1991 period.

Table 2. Cloud Perturbations to MSU Channels 2R, 2, and 3R T_b

Cloud Type	τ_{vis}	LWC, g/m	Surface	ΔT_b , K Channel 2	ΔT_b , K Channel 2R	ΔT_b , K Channel 3R
Tropics nimbostratus						
$r_{\text{eff}} 10 \mu\text{m}$	18	0.25	ocean	-0.12	-0.13	-0.03
$r_{\text{eff}} 7 \mu\text{m}$	25	0.25	land	-0.25	-0.40	-0.03
610–575 hPa 275–271 K						
Midlatitude nimbostratus						
$r_{\text{eff}} 10 \mu\text{m}$	18	0.25	ocean	-0.12	-0.13	0.03
590–555 hPa 260–257 K			land	-0.25	-0.41	-0.03
Tropics stratus						
$r_{\text{eff}} 10 \mu\text{m}$	20	0.25	ocean	0.07	0.17	-0.01
800–755 hPa 287–285 K			land	-0.09	-0.19	-0.01
Midlatitude stratus						
$r_{\text{eff}} 10 \mu\text{m}$	20	0.25	ocean	0.06	0.15	-0.01
790–740 hPa 275–271 K			land	-0.10	-0.19	-0.01
Tropics stratus						
$r_{\text{eff}} 10 \mu\text{m}$	18	0.25	ocean	0.12	0.26	0.00
950–900 hPa 297–293 K			land	-0.02	-0.04	0.00
Midlatitude stratus						
$r_{\text{eff}} 10 \mu\text{m}$	18	0.25	ocean	0.10	0.22	0.00
945–895 hPa 285–281 K			land	-0.02	-0.04	0.00

LWC, liquid cloud water content; r_{eff} , effective radius of cloud's droplet size distribution; τ_{vis} , cloud's visible opacity.

in the winter hemisphere and at higher latitudes. At first glance the muted nature of MSU channels 4 and 3R's mean annual maps would seem to be an excellent backdrop for observations of in situ supersonic aircraft impacts. However, MSU channel 4 shows the largest magnitudes of interannual variability, and channel 3R values are not yet available. Channel 4 captures the influence of planetary waves, volcanic eruptions such as El Chichon (1982) and Mount Pinatubo (1991), and sudden stratospheric warming episodes in its maps of mean annual temperatures and variability in Figure 3. *Randel and Cobb* [1994] found strong coherent variation in total ozone mapping spectrometer (TOMS) and MSU channel 4 data, especially in periods after volcanic eruptions. Channel 3R interannual variability maps are not yet available. Channel 2 and 2R T_b variabilities are particularly sensitive to El Niño-Southern Oscillation events in the tropics and over the central Pacific [*Yulaeva and Wallace, 1994*].

These simultaneous observations of mean temperature structures and variability at different altitudes will serve as the background for any anomalous climate signals. The interannual variability observed by MSU channels 2R, 2, and 4 serve as the natural "noise" which the GCMAM microwave signals are contrasted against in modeled signal-to-observed-noise (S/N) ratios. Such "higher-order" information from the MSU channels adds value to assessments of supersonic aircraft emissions' signals against the noise of natural variability.

4. Microwave Postprocessor

The radiative transfer postprocessor produces maps of microwave brightness temperatures with the GCMAM's global, annual-average fields of atmospheric and surface diagnostic parameters, that is, maps a microwave sounder would measure if flown over a GCMAM atmosphere. This microwave model

initially served as a postprocessor or "satellite" model to the GISS atmospheric general circulation model (GCM) [*Hansen et al., 1983*]. Only minor development was needed for the radiative transfer postprocessor to work with GCMAM fields. Figure 2 shows the insensitivity of MSU T_b to conditions in GCMAM layers above 3 hPa. Detailed discussion of the microwave radiative transfer model is given by *Shah and Rind* [1995].

GCMAM T_b maps are calculated assuming a nonscattering, refracting atmosphere containing absorbing molecular oxygen and water vapor in local thermodynamic equilibrium above a spectrally gray, Lambertian surface. Nonnegligible scattering from precipitation and large convective ice particles is ignored as such scattering events were filtered out of the MSU climatologies. Radiation is ray traced, and absorption is calculated for vertical layers of 20 hPa thickness below the 50-hPa level and layers of 5 hPa thickness above the 50-hPa level. This vertical resolution in the microwave model is finer than that used by *Shah and Rind* [1995] with the 9- and 18-layer GISS GCM. Surface emissivities range from 0.5 for an ocean surface, 0.70 for an ice-covered ocean, 0.85 for snow-covered land, and 1.00 for land. Intermediate values for surface emissivities are possible as grid cell coverage by a combination of surface types is incorporated into the final emissivity assigned to a cell.

Atmospheric opacity in the radiative transfer model comes primarily from the 33 molecular oxygen absorption resonances in the 60-GHz band. Additional opacity arises from continuum oxygen absorption, wing absorption by the oxygen 118-GHz line, seven water vapor lines between 22 and 752 GHz, and continuum water vapor absorption. The 60-GHz oxygen band requires careful line-by-line summation. Its absorption band-shape actually narrows with increasing pressure due to overlap and then interference of the individual O_2 lines with increasing

pressure [Rosenkranz, 1993]. This adds an additional interference term to the usual Van Vleck-Weisskopf lineshape expression for a summed resonant absorption. Recently improved oxygen coefficients based on new laboratory measurements have been incorporated into the microwave model [Liebe *et al.*, 1992].

5. Supersonic Aircraft Microwave Signals

GCMAM microwave responses in the MSU channels are presented as microwave signals and as signal-to-noise ratio in order to assess the significance of the supersonic emission's climatic impacts. The GCMAM's microwave signal from each perturbation is ΔT_b , an experiment's T_b minus the control run's average T_b over similar time periods in a given frequency channel. The signal-to-noise (S/N) ratio for each perturbation scenario is ΔT_b divided by the observed MSU variability in a given frequency channel. The exaggerated exhaust experiments' (Table 1) responses with varying SSTs are apparent in a single year's microwave emission. The more realistic exhaust experiments with varying SSTs require analysis of 5 individual years relative to the control run's 5-year average for a clearer assessment of a signal. Rind and Lonergan's [1995] "flagship" paper analyzed GCMAM diagnostics in detail for years 16–20 and 26–30 (which had similar responses) for the realistic ozone experiment and for years 26–30 and 46–50 (which had opposing responses) for the realistic water vapor experiment. This microwave analysis examines the same representative sets of years.

As shown below, GCMAM microwave maps do show strong microwave signals from the exaggerated exhaust forcings of zero ozone and doubled water vapor abundances. These signals from the exaggerated exhaust experiments could easily be detected despite natural microwave variability in the MSU channels. From the more realistic exhaust experiments, GCMAM microwave maps show dissimilar, less detectable microwave responses to the 2015 fleet's water vapor and ozone perturbations. Feedbacks from sea ice, snow cover, and cloud cover often overwhelm the impact of direct radiative forcings by the slighter water vapor and ozone changes.

These GCMAM simulations are equilibrium responses and are not the foreseen response of the climate in the year 2015. Instead, a time lag of roughly 30–40 years would be needed to reach these equilibrium responses given the employed ocean mixed layer. Thorough discussion of the GCMAM dynamical and climatic responses to exaggerated and realistic exhaust forcings is given by Rind and Lonergan [1995].

5.1. Ozone Microwave Signals

In the first exaggerated perturbation experiment, ozone in the lower stratosphere was removed without permitting sea surface temperature to change. This resulted in in situ cooling of ≤ 10 K in the tropical lower stratosphere and warming of ≤ 5 K in the middle stratosphere [see Rind and Lonergan, 1995, Figure 1]. Tropospheric-stratospheric vertical stability decreases with intense cooling in the lower stratosphere, forcing increased tropospheric and lower stratospheric eddy energy and $\sim 10\%$ amplified residual circulation in the lower stratosphere.

Both the high- and low-level clouds increase with increased eddy energy above 300 hPa, in contrast to expectations from previous climate model experiments. Generally, climate models have increasing low-level clouds and decreasing high-level

Table 3. Globally Averaged Annual Changes in GCMAM Ozone Experiments

Diagnostic	Zero Ozone	Realistic Ozone	Standard Deviation
Surface temperature, °C	-1.13	0.03	0.09
Absorb shortwave radiation at top of atmosphere, $W m^{-2}$	-2.6	-0.25	0.24
Net longwave radiation at top of atmosphere, $W m^{-2}$	-2.5	0.10	0.21
Evaporation, % relative	-2.3	0.20	0.44
Specific humidity, % relative	-8.9	0.40	0.80
Ground albedo, % absolute	0.29	-0.01	0.04
Planetary albedo, % absolute	0.86	0.07	0.07
Snow cover, % relative	6.9	0.00	0.86
Sea ice, % relative	5.7	-1.80	0.73
Total clouds, % absolute	2.0	0.18	0.27
High clouds, % absolute	2.5	0.17	0.61
Low clouds, % absolute	0.5	0.11	0.50
Tropospheric EAPE, % relative	7.1	0.20	0.7
Tropospheric EKE, % relative	6.0	-0.40	1.2
Lower Stratospheric EKE, 100–50 hPa layer, % relative	21.9	0.34	1.5

EAPE, eddy available potential energy; EKE, eddy kinetic energy. Table partly adapted from Rind and Lonergan [1995].

clouds coverage with a cooled climate (and opposite cloud coverage changes with a warmed climate). With both high and low cloud coverage increasing, this exaggerated supersonic aircraft forcing differentiates itself from the better known, future anthropogenic forcing of doubled CO_2 .

With sea surface temperatures permitted to respond, removal of ozone cooled global annual-average surface air temperatures by 1.13 K relative to the control run standard deviation of 0.09 K. This near-surface cooling occurs through decreased ozone greenhouse warming, reduced tropospheric water vapor, and increased sea ice, snow cover, and low cloud cover. Table 3 lists globally averaged changes in GCMAM diagnostics averaged over the last 5 years of the exaggerated ozone experiment, including eddy energy values. These changes in GCMAM diagnostics are very significant, being at least 5–10 times the interannual standard deviations from 30 years of the control run.

Figure 4 shows the ΔT_b signal (left) and the $\Delta T_b/MSU \sigma$ ratio (right) for the exaggerated ozone experiment (with sea surface temperatures allowed to adjust). Removal of stratospheric ozone and its greenhouse capacity dramatically cools the entire GCMAM atmosphere measurable by MSU channels. In particular, the lower stratosphere's channel 4 T_b values fall the most by 8.3 K in the tropics and reach high signal-to-noise ratios of 20. Cool departures to microwave T_b diminish in size for altitude regions closer to the surface and farther from levels of exhaust release. Similarly, strongest S/N ratios occur in the lower stratosphere at the pressure levels of ozone reduction between 200 and 50 hPa. These S/N ratios weaken with decreasing altitude, despite the maximum observed T_b variability in MSU channel 4.

In the realistic ozone perturbation case the stratosphere mostly cooled by a few tenths K due to infrared and solar heating decreases. Only over the poles does some stratospheric warming ≤ 2 K occur. This stratospheric warming arises through circulation changes via reduction in static stability due to middle-atmospheric cooling and thus increased planetary wave energy for the longest waves. This response follows the pattern found in the exaggerated ozone experiment, but total

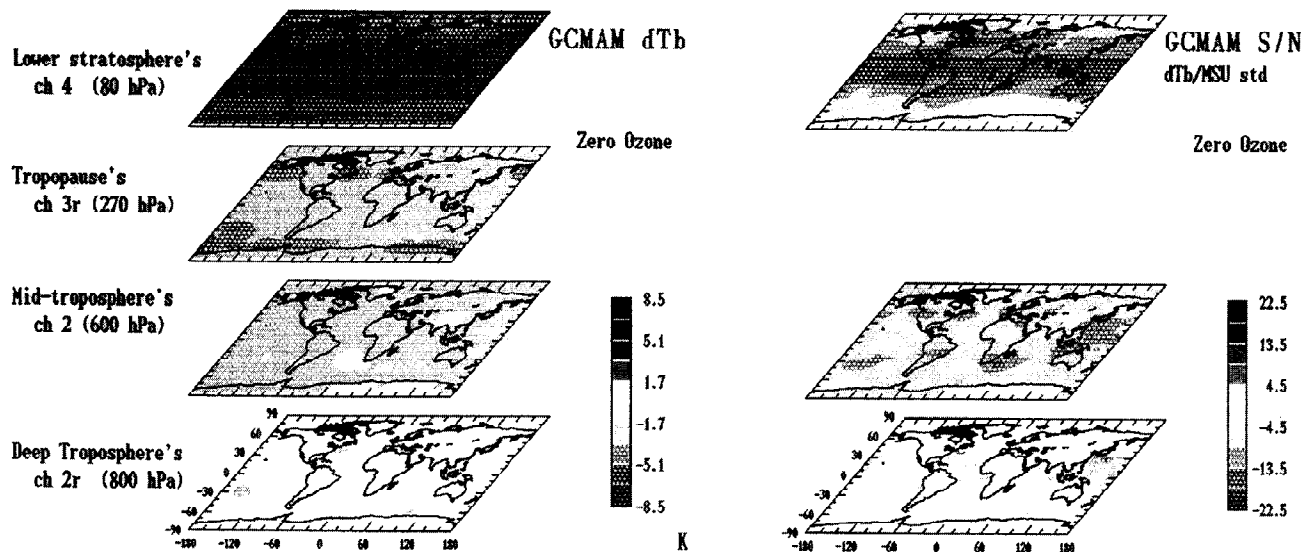


Figure 4. (left) ΔT_b , the microwave signals in the MSU channels, from the exaggerated ozone exhaust experiment (with sea surface temperatures allowed to adjust). Coldest ΔT_b values appear in the lower stratosphere's channel 4 map. T_b departures of ~ 8 K occur in the lower stratosphere with the removal of greenhouse warming through the removal of ozone between 200 and 50 hPa. (right) $\Delta T_b/\text{MSU } \sigma$, the microwave signal-to-noise (S/N) ratios, from the exaggerated ozone exhaust experiment. Positive (negative) S/N ratios indicate that the microwave signal was a warm (cold) departure from the control run T_b value. Removal of ozone is easily detected at perturbed altitudes in the lower stratosphere based on these results with S/N ratios of ~ 20 in channel 4.

stratospheric changes in eddy energy values amounted to $\leq 8\%$. Global surface air temperature changes were insignificant due to opposing influences. Stratospheric ozone reductions diminish infrared radiation downwelling into the troposphere but enhance solar radiation reaching the surface. Tropospheric ozone increases also warm the surface. Thus surface air temperatures responded to small, opposing forcings.

Table 3 lists globally averaged changes in GCMAM diagnostics averaged over the last 5 years of the realistic ozone experiment. These average responses by the GCMAM are not significant relative to the interannual standard deviations from the control run.

Figure 5 shows the zonal average ΔT_b values for the last 5 individual years of the realistic ozone GCMAM experiment. Zonal averaging is necessary in order to pull out a viewable signal ΔT_b . Nonetheless, the latitude-versus-time map of Figure 5 employs only a -1.5 – 1.5 K scale. A 1 K warm signal occurs over northern polar latitudes, and warm signals occur in the southern polar latitudes in the lower stratospheric channel 4 map, both associated with the above-mentioned dynamical changes. However, the realistic ozone perturbations generally force only scattered, small T_b departures of ≤ 0.6 K in all channels. None of the realistic ozone perturbation's microwave signals are detectable against observed MSU variability given their inconsistent distribution and small values. A S/N ratio map, if shown, would have bland ratios ≤ 1 across every channel map, excepting the polar warmth in the lower stratosphere. These polar warm signals in channel 4, overwhelmed by the high variability of this channel at high latitudes (Figure 3), also only achieve localized S/N ratios of ≤ 2 spread above North America to Europe.

5.2. Water Vapor Microwave Signals

In the exaggerated supersonic water vapor exhaust experiment, doubling stratospheric water vapor to 6 ppmv heightened the infrared radiating ability of the middle atmosphere. The amplified infrared action overrode the slight increase of solar absorption. This cooled middle-atmosphere temperatures by 2–3 K while warming upper tropospheric temperatures by ~ 0.5 K. The resulting decrease in tropospheric-stratospheric vertical stability enhanced tropospheric planetary wave activity by 10% for longest wave energy and enhanced stratospheric residual circulation by 5%. Stability increased within the troposphere, reducing the Hadley circulation by $\leq 10\%$ and consequently muting tropical precipitation while heightening subtropical precipitation. The surface feedbacks and the surface air temperature response of warming by a few tenths of a degree were diminished by the high altitudes of the aircraft forcing. The surface response was also diminished by a reduction in high cloud cover and greenhouse capacity due to upper tropospheric warming, reducing the relative humidity.

Table 4 lists globally-averaged changes in GCMAM diagnostics averaged over the last 5 years of the exaggerated water vapor experiment. Some of these changes in GCMAM diagnostics, such as surface air temperature, tropospheric specific humidity, and snow/sea ice cover, are significant relative to the interannual standard deviations from the last 30 years of control run in Table 3.

Microwave maps in Figure 6 highlight the impact of doubling of the middle atmosphere's ambient water vapor abundances with its warmed troposphere and cooled stratosphere. As expected, the impact of 6 ppmv H_2O above 100 hPa is strongest in channels measuring altitude regions near the

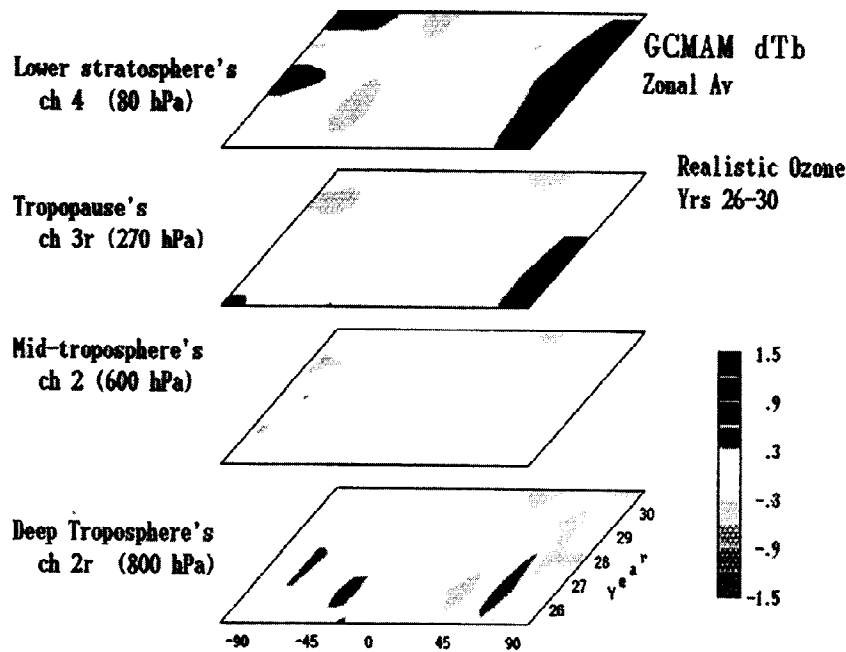


Figure 5. ΔT_b , the microwave signals in MSU channels, from the realistic ozone exhaust experiment (with sea surface temperatures allowed to adjust) are shown on the left as zonal averages for the last 5 years, years 26–30, of the experiment. Latitude runs along the horizontal axis, while time runs along the vertical axis. The ozone perturbations and ambient ozone abundances are shown in Figure 1.

tropopause [Rind and Lacis, 1993]. Cooling of the lower stratospheric channel 4 T_b values exceeds -1.5 K in the southern high latitudes and has associated S/N ratios of 1–2, spread from the northern subtropics to the southern polar latitudes in Figure 6. The warm response appears best in the upper troposphere's tropics with channel 3R ΔT_b values above $+1.0$ K. Warm signals also appear in the midtropospheric and lower tropospheric channels but with decreasing strength and areal coverage given greater distance from the forcing. Nonetheless, the tropospheric channel 2 and 2R S/N ratios indicate warming detectable above natural microwave variability with ratios of 2–4 across the tropics and the subtropics due to the perturbed Hadley circulation.

As seen in Figure 6, maps of simultaneous microwave signals

Table 4. Globally Averaged Annual Changes in GCMAM Water Vapor Experiments

Diagnostic	Doubled H ₂ O	Realistic H ₂ O (26–30)	Realistic H ₂ O (46–50)
Surface temperature, °C	0.24	-0.24	0.32
Absorb shortwave radiation at top of atmosphere, W m ⁻²	0.19	-0.68	0.59
Net longwave radiation at top of atmosphere, W m ⁻²	0.00	-0.51	-0.53
Evaporation, % relative	0.5	-1.0	1.5
Specific humidity, % relative	2.0	-1.8	2.7
Ground albedo, % absolute	-0.05	0.06	-0.11
Planetary albedo, % absolute	-0.06	0.20	-0.17
Snow cover, % relative	-1.3	2.0	-1.8
Sea ice, % relative	-1.8	0	-2.4
Total clouds, % absolute	-0.04	0.29	-0.09
High clouds, % absolute	-0.16	0.07	0.03
Low clouds, % absolute	-0.05	0.35	-0.22

Table adapted from Rind and Lonergan [1995].

at separate altitudes spotlight a climate's atmospheric lapse rate. These GCMAM increased water vapor experiments do predict a decreased tropospheric lapse rate: The doubled stratospheric water does preferentially warm the upper troposphere relative to lower-altitude atmospheric regions. Rind and Lonergan [1995] noted that this decreased atmospheric lapse rate occurred both in the doubled water vapor experiment with sea surface temperatures adjusting (i.e., feedbacks are occurring) and the experiment without sea surface temperatures adjusting (i.e., feedbacks are not occurring). These results are pertinent to one-dimensional radiative-convective models and assumed lapse rates during their climate experiments.

In the realistic $+0.2$ ppmv-water vapor experiment, middle atmospheric temperatures cooled by ≤ 0.5 K throughout the run's 50 years, echoing the exaggerated doubled-water vapor experiment. However, near the surface the response to realistic forcing differed from the stable, warmed-surface air temperature response of the exaggerated experiment. Surface temperature changes due to the realistic forcing varied in sign over the course of the simulation. The last decade in the realistic water vapor run showed a surface warming in contrast to the initial 40 years of net cooling. Also, the last decade ended with negative values for net radiation at the model's top, heralding a return to cool surface conditions [see Rind and Lonergan, 1995, Figure 18]. Changes in ground albedo, planetary albedo, shortwave radiation absorbed at the top of the atmosphere, evaporation, specific humidity, and snow and sea ice cover alternated in sign, consistent with surface warming or cooling. Therefore two extreme sets of years, cooling years 26–30 and warming years 46–50, from the realistic water vapor experiment are contrasted by Rind and Lonergan [1995] and here in terms of their microwave signals.

The GCMAM experiment forced by realistic supersonic water vapor amounts emphasized the strength and variability of

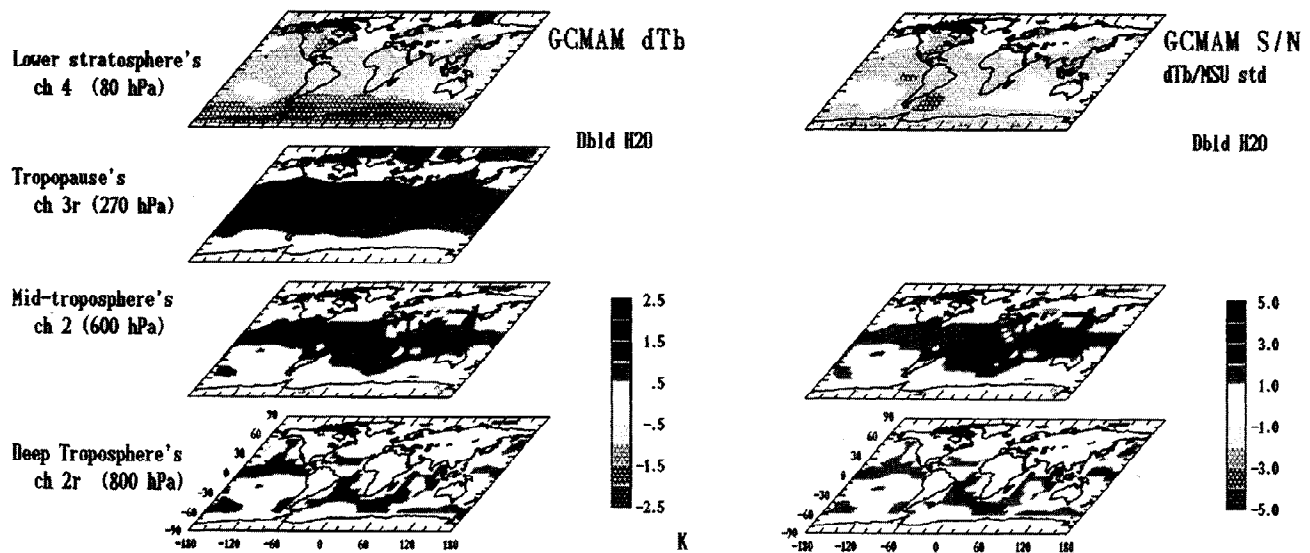


Figure 6. (left) ΔT_b , the microwave signals in the MSU channels, from the exaggerated water vapor exhaust experiment (with sea surface temperatures allowed to adjust). Doubling of water vapor above 100 hPa impacts T_b , particularly in the upper troposphere and lower stratosphere as expected [Rind and Lacs, 1993]. Warm departures of ≥ 1 K occur in channel 3R, and in the southern high latitudes, cold departures of ≥ 1 K occur in channel 4. (right) $\Delta T_b/\text{MSU } \sigma$, the microwave signal-to-noise ratios, from the exaggerated water vapor exhaust experiment. S/N ratios are shown in a manner similar to that in Figure 4. Of the available channels, MSU's midtropospheric channel best detects predicted impacts of exaggerated water vapor exhaust with S/N ratios of ≥ 3 over a wide area in the southern subtropics.

feedbacks. These feedbacks overwhelmed the slighter, direct radiative forcing by +0.2 ppmv water vapor injected at high altitudes. Tropospheric responses were controlled by feedbacks, not by aircraft forcing, as outlined in Table 4. Additional stratospheric water vapor should increase thermal emission and set up a positive net radiation balance at the top of the atmosphere (with more radiation entering the system, than leaving). Yet low clouds direct the net radiation through the run [see Rind and Lonergan, 1995, Figure 18]. These low clouds tend to decrease in a warmed climate with increased convection and moisture transport out of the boundary layer. But other processes, such as eddy energy, evaporation, and Hadley cell variations, can match or surpass warmed-climate processes. In this realistic forcing experiment, low-cloud variations via the planetary albedo steer the net radiation which, in turn, shapes the temperature response during the 50-year run. Table 4 quantifies the extreme responses with changes in low clouds and planetary albedo, and thus surface temperature, switching signs for years 26–30 versus 46–50.

Larger microwave signals, shown in Figure 7, are generated from the realistic water vapor forcing than from the realistic ozone forcing (Figure 5). The realistic water vapor T_b signals are still rarely above 0.6 K but clearly depict the warmed and cooled extremes in tropospheric response. The lower stratosphere does undergo stronger T_b departures of 1.2 K due to dynamical changes similar to those in the exaggerated water vapor experiment. However, these stronger signals occur at high latitudes, where natural microwave variability is largest, and, consequently, do not produce appreciable S/N ratios in Figures 7. The warm period of 46–50 from the realistic water vapor experiment does produce possibly detectable S/N ratios of 3–4 in the subtropics. These subtropical signals arise though a perturbed Hadley circulation. However, the usefulness of this

result is doubtful since tropospheric warming was inconsistent during 50-year simulation.

6. Summary and Conclusions

These results indicate that “realistic” supersonic fleet exhausts will produce small microwave signals. These slight signals may be conflicting and difficult to detect against natural variability and other sources of anthropogenic forcing. Overall, the realistic stratospheric ozone and water vapor perturbations produced ΔT_b signals below 0.6 K in all of the MSU channels, and these exhaust signals were not detectable relative to the observed MSU interannual variability. In both exhaust experiments, feedbacks, such as cloud coverage, sea ice and snow coverage, etc., overwhelm the slight direct forcings by the stratospheric, realistic exhaust.

However, this conclusion is subject to the possibilities that current, realistic exhaust constituents may be underestimated or inaccurately distributed by current photochemical models. Also, this conclusion is subject to the assumption that observed MSU interannual variability over the 1982–1990 period is representative of a future, perturbed climate’s microwave variability. Finally, this conclusion is subject to the simplified nature of the modeled exhausts herein and the GCMAM’s current parameterizations of cloud cover formation, sea ice formation, ocean transport, etc.

The exaggerated supersonic exhaust experiments produce microwave signals which would be easily detected against natural “noise” with current MSU capabilities. Removal of ozone between 200 and 50 hPa and its greenhouse capabilities cools T_b values in all of the MSU channels: Largest ΔT_b values of 8.3 K occur in the lower stratospheric channel, and decreasing ΔT_b values show up in channels measuring altitudes closer to

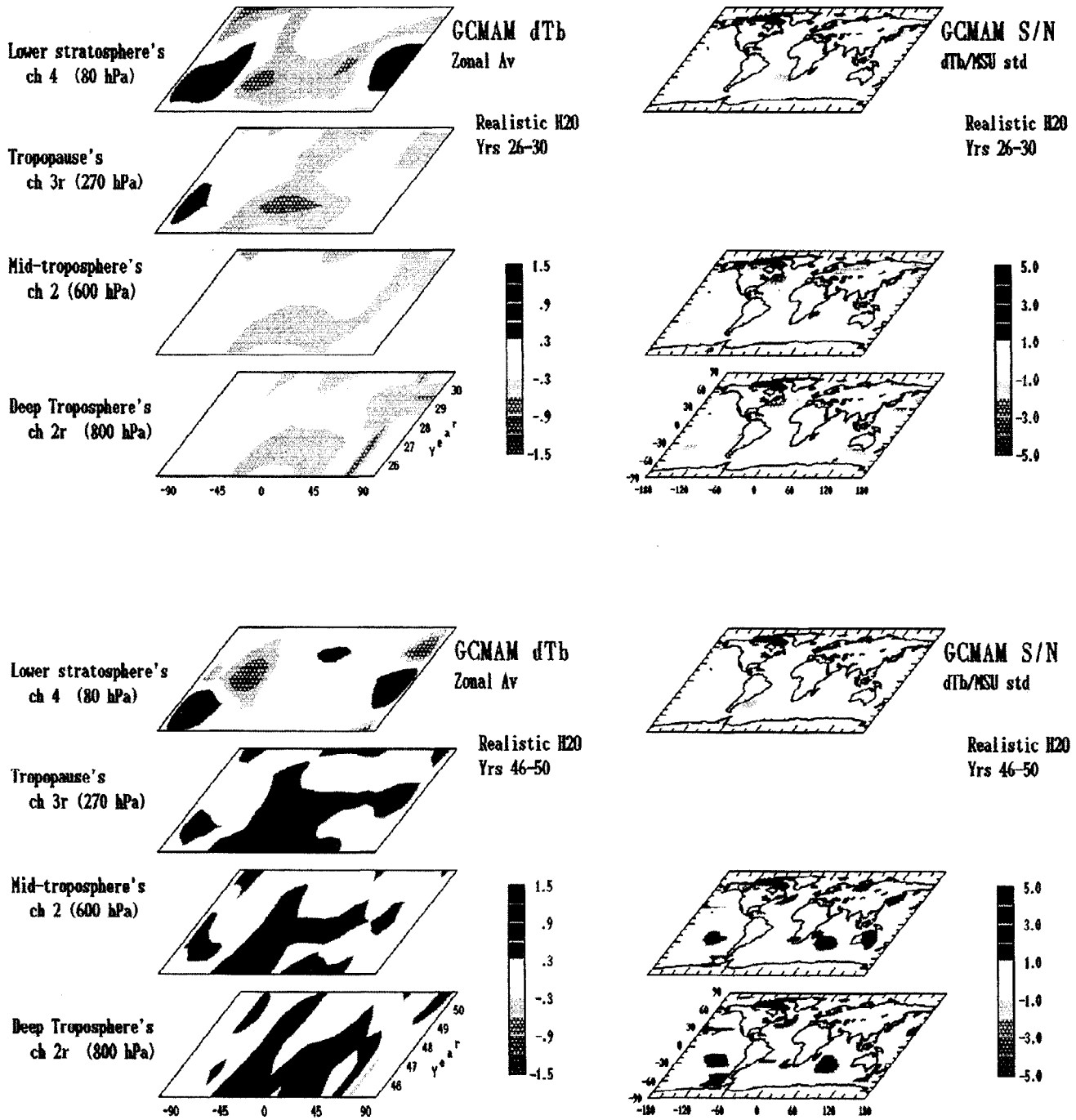


Figure 7. (top left) ΔT_b , the microwave signals in MSU channels, from the realistic water vapor exhaust experiment (with sea surface temperatures allowed to adjust) are shown as zonal averages for the 5 years, years 26–30, of the experiment. (bottom left) ΔT_b for the contrary, last 5 years, years 46–50. Latitude runs along the horizontal axis, while time runs along the vertical axis. $\Delta T_b/\text{MSU } \sigma$, the microwave signal-to-noise-ratios, from the realistic water vapor exhaust experiment for (top right) years 26–30 and for (bottom right) years 46–50. S/N ratios are shown in a manner similar to that of Figure 4.

the ground and farther from the dominant, in situ radiative forcing in the lower stratosphere. Signal-to-noise ratios, formed with the GCMAM's predicted ΔT_b values and the observed MSU interannual standard deviations, reach strikingly high values above 20 in the lower stratospheric channel with ozone removal. The other exaggerated exhaust experiment, doubling middle-atmosphere water vapor amounts above 100 hPa, also produced detectable signals: Cool ΔT_b of

≤ -1.5 K occur in the lower stratospheric channel, and warm signals occur in the tropospheric channels, particularly the upper tropospheric channel 3R with ΔT_b of ≥ 1.0 K.

The GCMAM simulates a complex nonlinear system. Thus a simple linearly scaled outcome for different exhaust amounts, lying between the realistic and exaggerated ozone and water vapor amounts modeled herein, could be misleading. Yet significant microwave signals might be detectable against natural

variability given some larger amount of “realistic” exhaust, an amount which need not be the exaggerated, climatically influential amounts tested in these GCMAM experiments.

If a linear scaling were possible, then these microwave results suggest that an amplification of the tested realistic ozone reduction (Table 1) by a factor of 10 (ozone reduction $\geq 15\%$ in the 200–50-hPa layer) would produce detectable S/N ratios ≥ 2 in lower stratospheric channel 4 T_b . Similarly, an amplification of the tested water vapor addition by a factor of 7 (water vapor increases ≥ 1.5 ppmv above 100 hPa) would produce detectable S/N ratios ≥ 2 in the tropics in midtropospheric channel 2 T_b . The complex coupling of mechanisms simulated by the GCMAM makes such linear-scaling results questionable at best. Therefore further long GCMAM simulations are appropriate with combinations of exhaust forcings including sulfur, soot, and CO₂ and with exhaust distributions in actual flight corridors. In future work, microwave analysis of modeled supersonic exhaust, subsonic exhaust signals, and greenhouse gas signals at MSU frequencies will lead to separation and intercomparison of anthropogenic impacts on our climate.

Acknowledgments. The authors thank Richard Stolarski for information on appropriate ozone changes and Roy Spencer and John Christy for producing these useful MSU climatologies. This research has been supported by the NASA Atmospheric Effects of Stratospheric Aircraft (AESA) High-Speed Research Program (HSRP). K. Shah has also been supported by the National Science Foundation Research Planning Grants Program under grant ATM 95-03277. Stratospheric modeling at GISS is supported by the NASA Atmospheric Chemistry Modeling and Analysis Program.

References

- Christy, J. R., and S. J. Drouilhet, Variability in daily zonal mean lower stratospheric temperatures, *J. Clim.*, **7**, 106–120, 1994.
- Goldberg, M. D., and H. E. Fleming, An algorithm to generate deep-layer temperatures from microwave satellite observations for the purpose of monitoring climate change, *J. Clim.*, **8**, 993–1004, 1995.
- Hansen, J., et al., Efficient three-dimensional global models for climate studies: Model I and Model II, *Mon. Weather Rev.*, **111**, 609–683, 1983.
- Hansen, J., A. Lacis, D. Rind, G. Russell, P. Stone, I. Fung, R. Ruedy, and J. Lerner, Climate sensitivity: Analysis of feedback mechanisms, in *Climate Processes and Climate Sensitivity*, *Geophys. Monogr. Ser.*, vol. 29, edited by J. Hansen and T. Takahashi, pp. 73–91, AGU, Washington, D. C., 1984.
- High-Speed Research Program/Atmospheric Effects of Stratospheric Aircraft (HSRP/AESA), The atmospheric effects of stratospheric aircraft: A third program report, *NASA Ref. Publ.*, **1313**, 413 pp., 1993.
- Lacis, A. A., D. J. Wuebbles, and J. A. Logan, Radiative forcing of climate by changes in the vertical distribution of ozone, *J. Geophys. Res.*, **95**, 9971–9981, 1990.
- Liebe, H. J., P. W. Rosenkranz, and G. A. Hufford, Atmospheric 60-GHz oxygen spectrum: New laboratory measurements and line parameters, *J. Quant. Spectrosc. Radiat. Transfer*, **48**, 629–643, 1992.
- McPeters, R., Ozone profile comparisons, vol. 2, *NASA Ref. Publ.*, **1291**, 1–37, 1993.
- Randel, W. J., and J. B. Cobb, Coherent variations of monthly mean total ozone and lower stratospheric temperature, *J. Geophys. Res.*, **99**, 5433–5447, 1994.
- Rind, D., and A. Lacis, The role of the stratosphere in climate change, *Surv. Geophys.*, **14**, 133–165, 1993.
- Rind, D., and P. Lonergan, Modeled impacts of stratospheric ozone and water vapor perturbations with implications for high-speed civil transport aircraft, *J. Geophys. Res.*, **100**, 7381–7396, 1995.
- Rind, D., R. Suozzo, N. K. Balachandran, A. Lacis, and G. L. Russell, The GISS global climate/middle atmosphere model, I, Model structure and climatology, *J. Atmos. Sci.*, **45**, 329–370, 1988a.
- Rind, D., R. Suozzo, N. K. Balachandran, A. Lacis, and G. L. Russell, The GISS global climate/middle atmosphere model, II, Model variability due to interactions between planetary waves, the mean circulation and gravity wave drag, *J. Atmos. Sci.*, **45**, 371–386, 1988b.
- Rind, D., R. Suozzo, N. K. Balachandran, and M. Prather, Climate change and the middle atmosphere, I, The doubled CO₂ climate, *J. Atmos. Sci.*, **98**, 475–494, 1990.
- Rind, D., N. K. Balachandran, and R. Suozzo, Climate change and the middle atmosphere, II, The impact of volcanic aerosols, *J. Clim.*, **5**, 189–208, 1992.
- Rosenkranz, P. W., Absorption of microwaves by atmospheric gases, in *Atmospheric Remote Sensing by Microwave Radiometry*, edited by M. A. Janssen, pp. 37–90, John Wiley, New York, 1993.
- Rosenkranz, P. W., K. D. Hutchison, and K. R. Hardy, Simulations of temperature retrieval accuracy in the middle and lower atmosphere using oxygen microwave lines, paper presented at Seventh Conference on Satellite Meteorology and Oceanography, Am. Meteorol. Soc., Monterey, Calif., June 6–14, 1994.
- Saunders, R. W., Note on the advanced microwave sounding unit, *Bull. Am. Meteorol. Soc.*, **74**(11), 2211–2212, 1993.
- Shah, K. P., and D. Rind, Use of microwave brightness temperatures with a general circulation model, *J. Geophys. Res.*, **100**, 13,841–13,874, 1995.
- Spencer, R., and J. Christy, Precision and radiosonde validation of satellite gridpoint temperature anomalies, I, MSU channel 2, *J. Clim.*, **5**, 847–857, 1992a.
- Spencer, R., and J. Christy, Precision and radiosonde validation of satellite gridpoint temperature anomalies, II, A tropospheric retrieval and trends during 1979–1990, *J. Clim.*, **5**, 858–866, 1992b.
- Yulaeva, E., and J. M. Wallace, The signature of ENSO in global temperature and precipitation fields derived from the microwave sounding units, *J. Clim.*, **7**, 1719–1736, 1994.

P. Lonergan, D. Rind, and K. P. Shah, Center for Climate Systems Research, Columbia University, NASA Goddard Institute for Space Studies, 2880 Broadway, New York, NY 10025. (e-mail: cdppl@nasagiss.giss.nasa.gov; cddhr@nasagiss.giss.nasa.gov; cakps@nasagiss.giss.nasa.gov)

(Received June 13, 1995; revised June 28, 1996; accepted June 28, 1996.)